








## Last deglacial abrupt climate changes caused by meltwater pulses in the Labrador Sea

Defang You <sup>1✉</sup>, Ruediger Stein <sup>1,2,3</sup>, Kirsten Fahl <sup>1</sup>, Maricel C. Williams<sup>4</sup>, Daniela N. Schmidt <sup>4</sup>, Ian Nicholas McCave<sup>5</sup>, Stephen Barker<sup>6</sup>, Enno Schefuß <sup>2</sup>, Lu Niu <sup>1</sup>, Gerhard Kuhn <sup>1</sup> & Frank Niessen<sup>1</sup>

Freshwater perturbations are often thought to be associated with abrupt climate changes during the last deglaciation, while many uncertainties remain regarding the exact timing, pathway, mechanism, and influence of meltwater release. Here, we present very well-dated and high-resolution records from the eastern Labrador Sea representing the last 19,000 years, which demonstrate abrupt changes in sea surface characteristics. Four millennial-scale meltwater events have been identified between the last 14,000 and 8,200 years based on independent biomarker proxies and X-ray fluorescence scanning data. These events are characterized by increased sea ice formation and decreased sea surface temperatures which might have occurred within a few decades. We propose these abrupt changes were triggered by meltwater pulsing into the Labrador Sea periodically, resulting from collapse of the Laurentide-Greenland Ice Sheets caused by (sub-)surface ocean warming in the Labrador Sea. Our findings provide more precise information about impact of freshwater forcing on abrupt climate changes, which may help to improve simulations for past and future changes in ocean circulation and climate.

<sup>1</sup> Alfred Wegener Institute Helmholtz Centre for Polar and Marine Research, Bremerhaven 27568, Germany. <sup>2</sup> MARUM-Center for Marine Environmental Sciences and Faculty of Geosciences, University of Bremen, Bremen 28359, Germany. <sup>3</sup> Frontiers Science Center for Deep Ocean Multispheres and Earth System, Key Laboratory of Marine Chemistry Theory and Technology, Ocean University of China, Qingdao 266100, China. <sup>4</sup> School of Earth Sciences, University of Bristol, Bristol BS8 1RJ, UK. <sup>5</sup> Godwin Laboratory for Palaeoclimate Research, Department of Earth Sciences, University of Cambridge, Cambridge CB2 3EQ, UK. <sup>6</sup> School of Earth and Environmental Sciences, Cardiff University, Cardiff CF10 3AT, UK. ✉email: [defang.you@awi.de](mailto:defang.you@awi.de)

Greenland ice cores preserve signals of atmospheric temperature fluctuations and reveal millennial-scale abrupt climate changes during the last glacial cycle<sup>1</sup>. These abrupt changes (known as Dansgaard-Oeschger, D-O cycles<sup>2,3</sup>) were pronounced during Marine Isotope Stage 3 and also occurred during the last deglaciation<sup>1,4</sup>. Modelling results suggest that these abrupt changes were related to intermediate or transitional climate states and closely associated with variations in the Atlantic Meridional Overturning Circulation (AMOC)<sup>5</sup>. Previous research has linked AMOC variations to direct external forcing (i.e., astronomical influence)<sup>6</sup> as well as internal feedback from the earth system, including changes in northern hemisphere ice sheet height, freshwater perturbations, and CO<sub>2</sub> levels, which can be related to variations in insolation caused by orbital changes<sup>5,7,8</sup>.

As an unstable transition characterized by abrupt climate changes, the last deglaciation contains several outstanding stadial stages such as Heinrich Stadial 1 (HS1), the Younger Dryas (YD) cold event, and the 8.2 ka BP cold event<sup>1,4</sup>. The occurrence of these cold episodes was often implicated with iceberg/meltwater discharge from the Laurentide Ice Sheet (LIS)<sup>9–12</sup>. As one of the major outlets of the LIS ice streams<sup>13</sup>, large numbers of iceberg/meltwater were transported through the Hudson Strait into the Labrador Sea during the last deglaciation<sup>14</sup>. Furthermore, the retreat of the Greenland Ice Sheet (GrIS) could also contribute to meltwater discharge into the Labrador Sea<sup>15–18</sup>. The freshwater from melted icebergs and land ice could have led to surface

freshening not only in the Labrador Sea<sup>19,20</sup> but may have extended over the wider North Atlantic subpolar area, as indicated from ice-rafted debris (IRD) records<sup>9,21</sup> (Fig. 1). This freshening may have caused reduced deep-water formation and limited ventilation in the North Atlantic<sup>7,22,23</sup>. However, many uncertainties remain regarding the exact timing, pathway, mechanism, and influence of meltwater discharge during the last deglaciation.

The Labrador Sea is an optimal area for reconstructing the history of meltwater discharge due to its proximity to the LIS and the GrIS. Furthermore, the sedimentation rates over Eirik Drift (in the eastern Labrador Sea) are high (average over 30 cm/kyr)<sup>24</sup> allowing high-resolution proxy-based reconstructions of meltwater discharge, and sea ice cover, etc. Compared to upstream areas under intense winnowing<sup>25</sup>, this area might also preserve a continuous record of the strength of bottom currents, which could be related to Denmark Strait Overflow Water (DSOW), the deepest component of North Atlantic Deep Water<sup>24</sup> (Supplementary Fig. 1).

Here, we have investigated a very well-dated and high-resolution sediment core from the Eirik Drift (Fig. 1), representing an interval from the last deglaciation to Holocene, i.e., the last 19 ka. During the last deglaciation, four meltwater events have been identified by abrupt changes in sea surface characteristics, which are based on independent multiple biomarker proxies (i.e., IP<sub>25</sub> and P<sub>D</sub>IP<sub>25</sub> for sea ice cover<sup>26,27</sup>, specific sterols and alkenones for open-water phytoplankton productivity<sup>26–28</sup>,

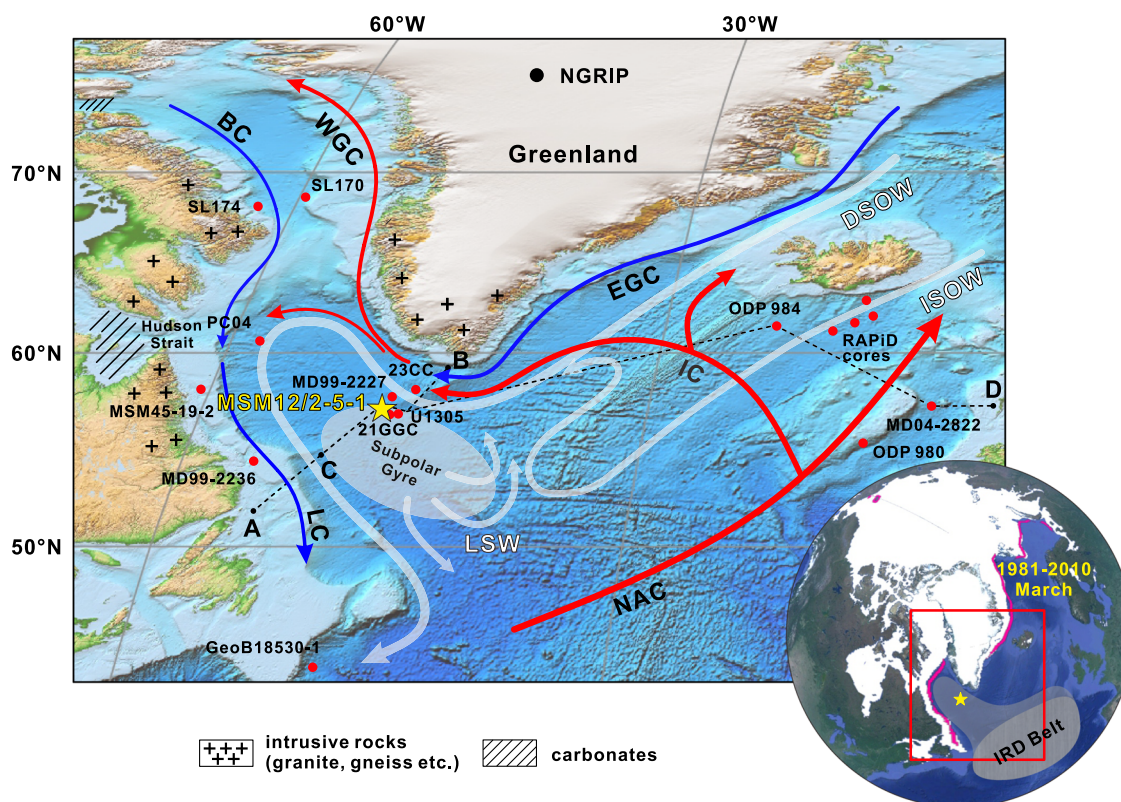


**Fig. 1 Core sites and regional context of the study area.** Main map with core sites and modern ocean circulation pattern. Yellow star: Core MSM12/2-5-1; red dots: other cores referred to; red arrows: warm surface currents; blue arrows: cold surface currents; white arrows: deep and intermediate currents. NAC North Atlantic Current, IC Irminger Current; WGC West Greenland Current, EGC East Greenland Current, BC Baffin Current, LC Labrador Current, DSOW Denmark Strait Overflow Water, ISOW Iceland-Scotland Strait Overflow Water, LSW Labrador Sea Water. Black stippled lines A to B and C to D show location of hydrographic transects presented in Supplementary Fig. 1. Simplified bedrock geology based on ref. <sup>87</sup>. Map was taken from ETOPO1 (source: <https://www.ngdc.noaa.gov/mgg/global/>). Small overview map (right lower corner) with average sea ice extent of 1981–2010 March (image modified from Google Earth, data source: <https://nsidc.org/>), IRD belt (dark grey shading)<sup>21</sup>, distribution range of cores with IRD signal around the Labrador Sea (light grey shading)<sup>88</sup>, and the study area (red box).

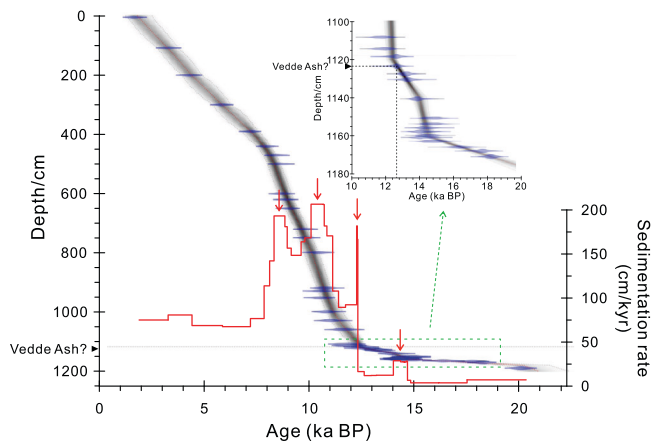


**Fig. 2 Age model of Core MSM12/2-5-1.** Bayesian age-depth model was established based on 38 radiocarbon dates (see Supplementary Table 1) using the Bacon program<sup>75</sup>. The horizontal dashed lines indicate sediment depths where sedimentation rates change significantly. Grey stippled lines indicate 95% confidence intervals of calibration age. The red line shows linear sedimentation rates (LSR) based on the calibrated age control points; red arrows highlight the intervals of maximum LSR. The black triangles mark the depth of a prominent tephra layer that probably represents the Vedde Ash layer<sup>32</sup>.

the alkenone unsaturation index  $U_{37}^K$  for sea surface temperature (SST)<sup>28</sup>, the percentage of tetra-unsaturated alkenones ( $\%C_{37:4}$ ) and stable hydrogen isotope composition of palmitic acid ( $\delta D_{PA}$ ) for meltwater discharge<sup>29,30</sup>, for details see Methods) and X-ray fluorescence (XRF) scanning data. Furthermore, sortable silt mean size has been used to reflect changes in bottom current intensity. In overall, enhanced Atlantic Water inflow may induce the (sub-)surface ocean warming and trigger collapse of the ice sheets surrounding the Labrador Sea. The following meltwater discharge potentially increased sea ice formation and promoted stratification of the upper ocean column in the Labrador Sea/subpolar area, preventing Atlantic Water inflow, and consequently disrupting the climate.

## Results

**Lithology, chronology and sedimentation rates.** During Expedition MSM12/2 of R/V *Maria S. Merian*, a 15m long Core MSM12/2-5-1 was recovered from the Eirik Drift at 57° 32.31' N, 48° 44.32' W in a water depth of 3491 m<sup>31</sup>. Here, we concentrate on the well-dated upper ~ 12 m of this core, representing the last 19 ka. The sediments are mainly composed of silty clay with intercalated grain-size related laminated intervals between 1103 and 1070 cm (12.2–11.8 ka BP), 992 and 940 cm (11–10.7 ka BP), 914 and 820 cm (10.6 to 10.2 ka BP), and 590 and 507 cm (8.7 to 8.3 ka BP), respectively (Supplementary Fig. 2 and X-ray photographs in Supplementary Fig. 3). A prominent maxima of tephra shards was found in the coarse fraction ( $>63 \mu\text{m}$ ) in 1123 cm core depth (corresponding to 12.6 ka BP according to our age model; Fig. 2) that may represent the Vedde Ash dated to 12.12 ka BP<sup>32</sup>. We have not used this date for the development of our age model (see Methods for details).

Based on our age model, the mean sedimentation rate is 106.7 cm/kyr in the upper 1118 cm and 10 cm/kyr in the lower 60 cm. Three intervals with peak sedimentation rates occur at 12.4–12.1 ka BP (181 cm/kyr), 10.7 to 10.1 ka BP (206 cm/kyr), and 8.9–8.3 ka BP (193 cm/kyr), respectively (Fig. 2). One other interval with higher sedimentation rates occurs at 14.8 to 13.9 ka BP (28 cm/kyr). This well-dated sedimentary sequence of Core MSM12/2-5-1 allows a detailed proxy-based reconstruction of the

environmental evolution in the Labrador Sea and its significance for (global) climate change during the last deglaciation.

## Changes in sea ice, sea surface temperature, and productivity.

The results of biomarker-based reconstruction of sea ice, SSTs, and primary productivity are shown in Fig. 3. Following Mollenhauer et al.<sup>33</sup>, radiocarbon age differences between biomarker (alkenones) and planktic foraminifera in records from the Gardar Drift (close to Eirik Drift) are negligible, suggesting that marine organic matter has been deposited quiet rapidly or only transported over very short lateral distance. Therefore, we interpret our biomarker records to reflect predominantly surrounding environmental conditions. Furthermore, we base our argumentation on the similarity of the alkenone-based SSTs with those derived from Mg/Ca ratios of planktic foraminifera (more likely to be in situ) (Fig. 3c), suggesting that the more-easily transported biomarker records are not affected by long-distance allochthonous transport. Finally, biomarker-based reconstructions from surface sediments in the Baffin Bay and the Labrador Sea mirror modern surface water and sea ice conditions very well<sup>34,35</sup>, therefore supporting our interpretation.

Several abrupt changes in surface characteristics occur during the last deglaciation. Around 18.4 ka BP, the sea ice extent decreased rapidly as shown by decreased values of sea ice proxy  $P_{DIP_{25}}$ , coinciding with the abrupt increase in SSTs. Temperatures based on both alkenones and planktic foraminiferal Mg/Ca show relatively high values (warmer than the modern annual average) during the early HS1 (Fig. 3c). During the late HS1, the  $P_{DIP_{25}}$  values are around 0.5, indicating marginal ice zone conditions ( $0.5 < P_{DIP_{25}} < 0.7$ ). Simultaneously increased concentrations of  $IP_{25}$  and open-water phytoplankton biomarkers (Fig. 3a, e, f) could be explained by polynya formation along the GrIS margin, caused by strong offshore katabatic winds at the edge of the extended ice sheets (cf., ref. 36). The maximum occurrence of HBI-III (Z) concentration may also support a marginal ice zone situation (cf., ref. 37). In addition to the late HS1, four prominent meltwater events have been identified (for details see below). These events are marked by abrupt increase in  $P_{DIP_{25}}$  values, decrease in the concentrations and accumulation rates of open-water phytoplankton indicators, decrease in SSTs, and low planktic foraminifera abundance, reflecting abruptly increased sea ice formation, reduced primary productivity, and strong meltwater discharge (cf., Fig. 4c). According to Müller et al.<sup>27</sup>, low concentrations of both  $IP_{25}$  and open-water phytoplankton biomarkers might point to permanent sea ice cover, prohibiting the growth of ice algae and open-water phytoplankton due to limited light and nutrient supply (Supplementary Fig. 4). However, SST values well above 0 °C in our record contradict this interpretation. Instead, oligotrophic conditions due to massive meltwater input seem to be a more realistic explanation of the reduced surface-water production in this case (cf., Fig. 4c).

During the middle to late Holocene (i.e., the last about 8 ka), the sea ice biomarker  $IP_{25}$  and the ice-edge related biomarker HBI-III (Z) are absent, but high contents of open-water phytoplankton biomarkers dinosterol and  $C_{37}$  alkenones are found, indicating an ice-free ( $P_{DIP_{25}} = 0$ ) and elevated surface-water productivity environment. The complete absence of HBI-III (Z) throughout this time interval characterized by the absence of any sea ice, is supporting that HBI-III (Z) is somehow related to sea ice (the marginal ice zone, see above) as proposed by Belt et al.<sup>37</sup>. The decreasing Holocene SST values reflected by both alkenones and Mg/Ca records, are probably driven by reduced summer insolation (Fig. 4a, e).

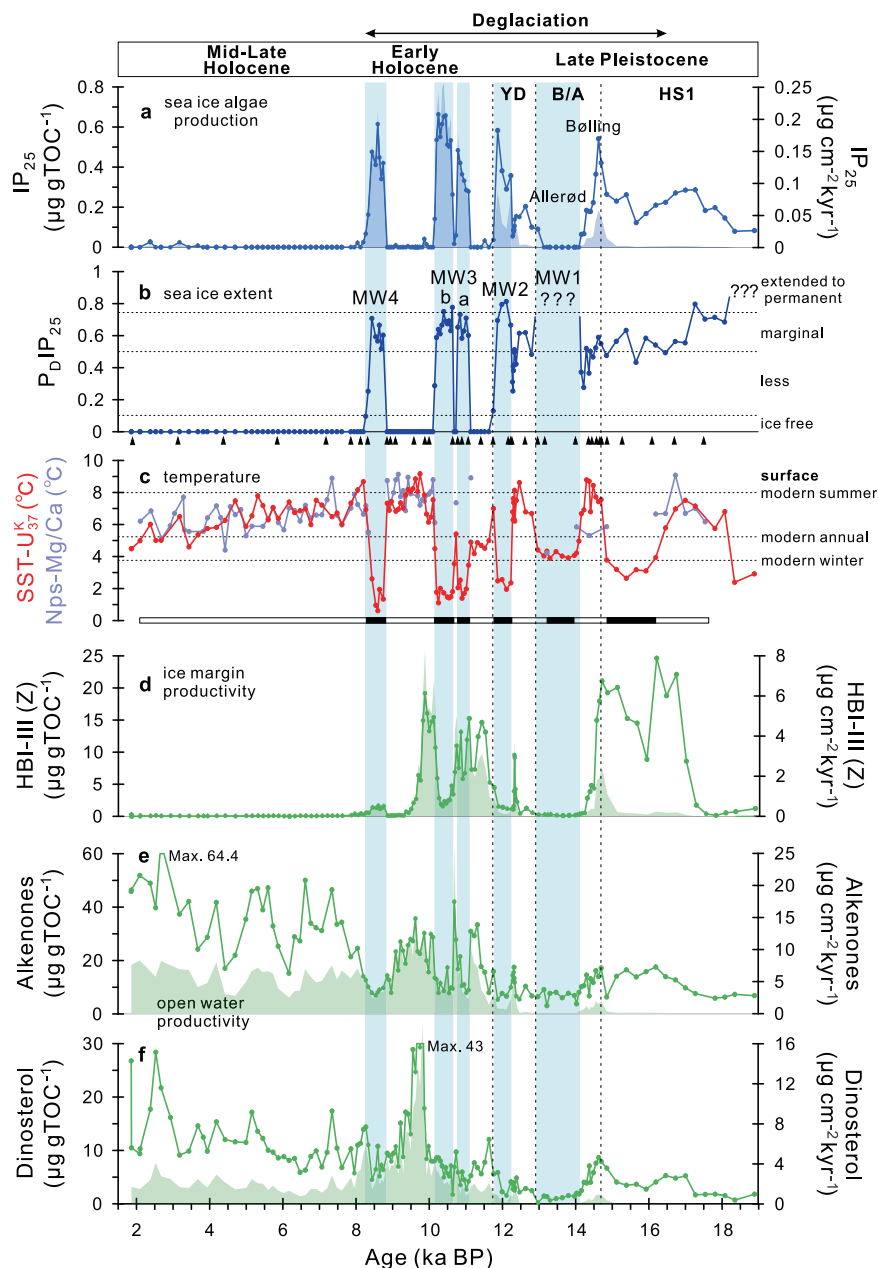


**Fig. 3** Proxy records for sea surface characteristics (Core MSM12/2-5-1). **a** Concentration (line) and accumulation rate (shading) of  $IP_{25}$ ; **b**  $P_{DI}IP_{25}$  based on dinosterol. For the intervals characterized by zero or minimum concentrations of  $IP_{25}$  and phytoplankton biomarkers,  $P_{DI}IP_{25}$  values cannot be calculated (highlighted by question marks; cf., Müller et al.<sup>27</sup>); for details see text and Supplementary Fig. 4; **c** Sea surface temperature (SST) based on  $U_{37}^K$  and *N. pachyderma* (sin.) (*Nps*)-Mg/Ca values. Black and white bar represents the abundance of planktic foraminifera, with black bars indicating intervals of absence or low abundance of planktic foraminifera (thus no Mg/Ca temperatures and  $\delta D_{PA}^{14}C$  could be determined), probably related to too low salinity due to strong meltwater discharge (cf., Fig. 4c); **d** HBI-III (Z); **e** Alkenones; **f** Dinosterol. Light blue shadings highlight the intervals of strong meltwater discharge. Vertical stippled lines mark the intervals: Heinrich Stadial 1 (HS1), the Younger Dryas (YD), and the Bølling/Allerød (B/A). Black triangles mark available  $AMS^{14}C$  dates.

**Changes in meltwater discharge.** We used the percentage of tetra-unsaturated alkenones ( $\%C_{37:4}$ ) as proxy for low temperature and/or low salinity conditions (i.e., meltwater input) (e.g., ref. 29). According to Prahl and Wakeham<sup>28</sup>,  $C_{37:4}$  is synthesized by *Emiliania huxleyi* (a dominant coccolithophorid species in seawater) at low temperatures but also other alkenone producers adapted to low salinity water<sup>29,38,39</sup>. More recently, Lochte et al.<sup>40</sup> and Wang et al.<sup>41</sup> have proposed that  $\%C_{37:4}$  might be an index for sea ice cover. Based on culture experiments<sup>41</sup>, this alkenones can also be produced by a newly found lineage of coccolithophorids living in sea ice, reaching  $\%C_{37:4}$  values around 80%. However,  $C_{37:4}$  is not

the dominant alkenones in our record (i.e.,  $<12\%$ ) (Fig. 4c), suggesting that open-water algae production influenced by meltwater is probably the primary source of alkenones here. In order to further support our argumentation that  $\%C_{37:4}$  is related to meltwater discharge, stable hydrogen isotope compositions of palmitic acid ( $\delta D_{PA}$ ) have been measured in selected samples. Although palmitic acid is produced by most marine and terrestrial organisms, Sachs et al.<sup>30</sup> presented multiple lines of evidence that support marine phytoplankton being its primary source to Arctic Ocean sediments. In their study of surface sediments along transects representing large salinity gradients from 11 to 32, these

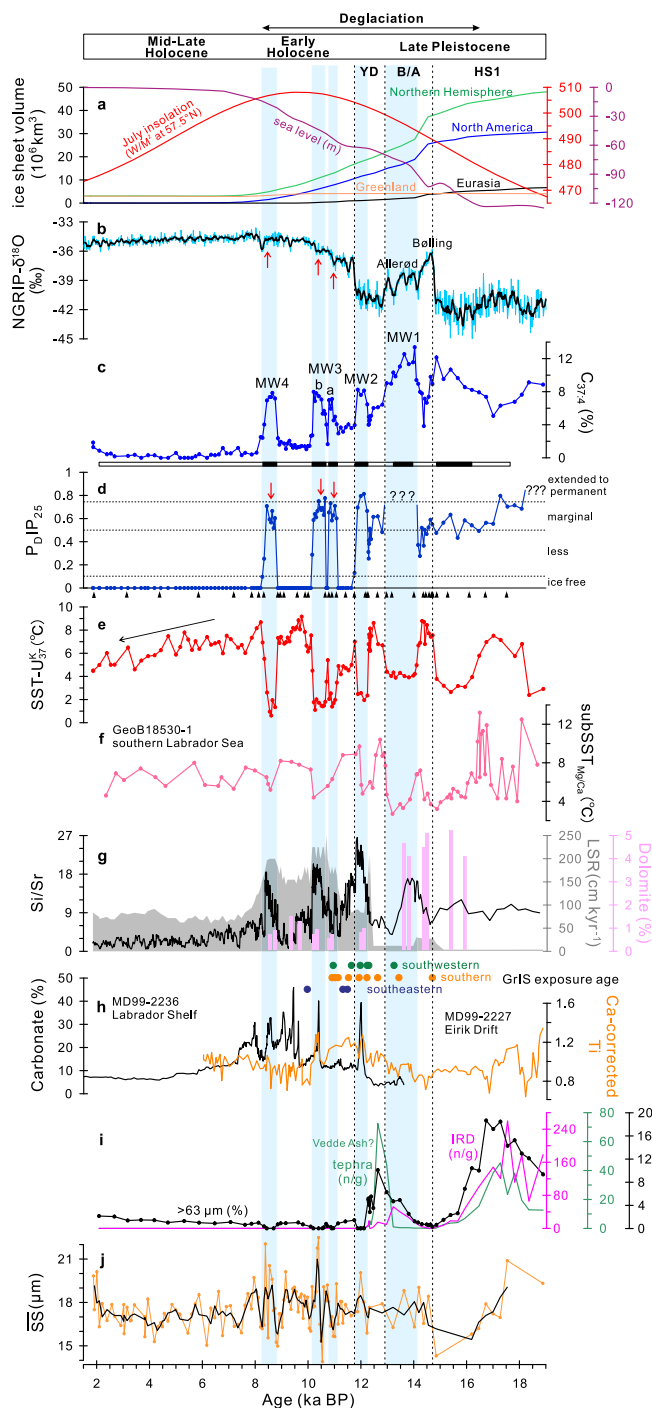


**Fig. 4 Proxy records of climate trends and abrupt climate changes during the last deglaciation.** **a** Changes in North Hemisphere ice sheet volumes<sup>89</sup>, global sea level<sup>72</sup>, and July insolation at 57.5° N<sup>90</sup>; **b** Greenland NGRIP- $\delta^{18}\text{O}$ <sup>4</sup>. The age of ice core was calculated from GICC05 age to cal. ka BP; **(c–e)** Proxies for abrupt changes from Core MSM12/2-5-1: **c** Percentage of  $\text{C}_{37:4}$  as proxy for meltwater discharge; black and white bars represents the abundance of planktic foraminifera, with black bars indicating intervals of absence or low abundance of planktic foraminifera; **d**  $\text{P}_{\delta}\text{IP}_{25}$  based on  $\text{IP}_{25}$  and dinosterol as proxy for sea ice extent (cf., Fig. 3b and Supplementary Fig. 4 for further explanation); red arrows indicate the intervals corresponding approximately to the cold phases in the ice core record during the early Holocene; **e** SST reconstruction based on  $\text{U}_{37}^k$ . Black arrow shows a decreasing trend following the decreasing insolation; **f** Subsurface temperature record based on Nps-Mg/Ca ratios from Core GeoB18530-1<sup>55</sup>; **g** Si/Sr ratios as proxy for detrital silicate input, linear sedimentation rates (LSR; grey shading), and dolomite content from Core MSM12/2-5-1. **h** Exposure ages based on  $^{10}\text{Be}$  indicating the decay of the GrIS<sup>15,16</sup>; detrital carbonate content from Core MD99-2236<sup>14</sup>; Ti record corrected against Ca from Core MD99-2227 indicating the runoff from the GrIS<sup>18</sup>; **i** Coarse fraction (>63  $\mu\text{m}$ ) content, IRD abundance, and tephra abundance from the Core MSM12/2-5-1; **j** Sortable silt mean size ( $\overline{\text{SS}}$ ) record as proxy for flow speed of bottom currents from Core MSM12/2-5-1; black line shows 3 points running average of  $\overline{\text{SS}}$  values. Age models of Core GeoB18530-1 and MD99-2236 have been recalculated based on Bacon program using “ $\Delta R = 0 \pm 200$ ” and “ $\Delta R = 50 \pm 50$ ”, respectively. Light blue shadings highlight the intervals of strong meltwater discharge. Vertical stippled lines mark the intervals: Heinrich Stadial 1 (HS1), the Younger Dryas (YD), and the Bølling/Allerød (B/A). Black triangles mark available AMS<sup>14</sup>C dates.

11.51–10.48 ka (95%); MW3b: 10.64–10.15 ka, 10.96–9.81 ka (95%); MW4: 8.74–8.33 ka, 9.05–8.01 ka (95%)) (Fig. 4c). The absence or low abundance of planktic foraminifera during meltwater events may also support low salinity in the upper ocean due to strong meltwater discharge (Figs. 3c, 4c). During the middle to late Holocene, i.e., the last about 8 ka, there is nearly no  $\text{C}_{37:4}$  (meltwater input) due to the complete decay (absence) of the LIS. The absence of meltwater may explain the dominantly ice-free conditions in the eastern Labrador Sea during this time interval. At around 2 ka BP, a slight increase in  $\% \text{C}_{37:4}$  values are probably associated with the Neoglacial expansion of the GrIS<sup>42</sup> which might have triggered some release of meltwater into the Labrador Sea.

There are probably two major sources of meltwater. One is from melted icebergs, which is characterized by increased ice-rafted debris (IRD) abundance. The other is meltwater plumes triggered by disintegration of ice sheets and characterised by high loading of fine-grained suspended matter<sup>43,44</sup>, as shown by increased  $\% \text{C}_{37:4}$  values, low percentage of coarse fraction (>63  $\mu\text{m}$ ), and low IRD abundance. During MW1, high  $\% \text{C}_{37:4}$  values and increased IRD abundance indicate increased iceberg discharge into the eastern Labrador Sea, a situation similar to the HS1. However, during MW2, MW3, and MW4, increased  $\% \text{C}_{37:4}$  values coinciding with extremely low coarse fraction content suggest freshwater/meltwater is released by meltwater plumes (Figs. 4i and 5c). The dominance of laminated silty clay/clayey silt deposits and the absence of coarse-grained IRD during MW2 to MW4 (see X-ray photographs in Supplementary Fig. 3; “plumites”) further demonstrate the importance of suspension-rich meltwater plumes controlling sedimentation at these times. Such pulses of suspended fine-grained detrital sediment input most likely contributed to high concentrations of the non-biogenic fraction and elevated sedimentation rates (Figs. 2, 4g). Increased silicon (Si) to strontium (Sr) ratios (an index for detrital silicate-rich minerals input<sup>45</sup>) and some dolomite deposition (Fig. 4g) suggest that these meltwater plumes are related to the LIS with transport via Hudson Strait, probably superimposed by input from the GrIS (Fig. 1).

authors demonstrate the correlation between the  $\delta\text{D}_{\text{PA}}$  values and surface water salinity, with low (high)  $\delta\text{D}_{\text{PA}}$  values indicating low (high) salinity sea surface environments. Thus, the good correlation between  $\% \text{C}_{37:4}$  and  $\delta\text{D}_{\text{PA}}$  values supports our interpretation as meltwater signal (Fig. 5a).

$\% \text{C}_{37:4}$  values are highly variable during the last deglaciation. Following the late HS1 interval with  $\% \text{C}_{37:4}$  values that gradually increased, four meltwater events have been identified that display abrupt and rapid increase in  $\% \text{C}_{37:4}$  values (i.e., meltwater discharge) within a few decades. We name these events MW1 to MW4, with MW3 comprising two phases (a and b) that maybe occur around 150 years apart (MW1: 14.08–12.93 ka based on median age, 14.62–12.67 ka (95% confidence interval); MW2: 12.23–11.87 ka, 12.52–11.45 ka (95%); MW3a: 11.07–10.78 ka,

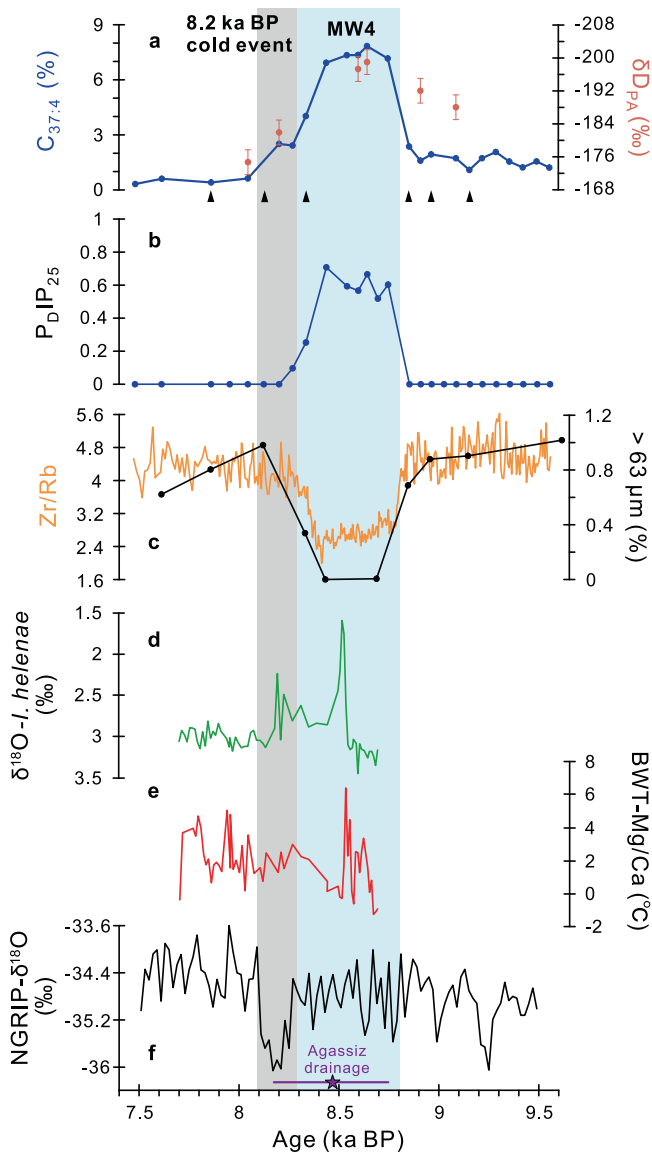


**Fig. 5 Proxy records of MW4 versus the 8.2 ka BP cold event.** **a–c** Proxy records for abrupt change during MW4 from Core MSM12/2-5-1. **a**  $\%C_{37:4}$  and stable hydrogen isotope composition of palmitic acid ( $\delta D_{PA}$ ) as proxies for meltwater discharge (with higher  $C_{37:4}$  and lower  $\delta D_{PA}$  representing lower salinity). Vertical error bars represent the standard deviation of the  $\delta D_{PA}$  measurements (3‰); **b**  $P_{DI} P_{25}$  as proxy for sea ice extent; **c** XRF-Zr/Rb ratios indicating coarse versus fine-grained matter; percentage of coarse fraction (>63  $\mu m$ ); **(d, e)** Proxy records for abrupt change around 8.5 ka BP from Core MSM45-19-2<sup>12</sup>. **d**  $\delta^{18}O$  of benthic foraminifera *Icelandella helenae*; **e** Bottom water temperature estimates based on Mg/Ca ratios of *I. helenae*. **f** Greenland NGRIP- $\delta^{18}O$ <sup>4</sup>. The age of ice core record was calculated to cal. ka BP from GICC05 age. The purple star indicates the age for Lake Agassiz drainage event: 8.47 ka BP with  $1\sigma$  uncertainties (purple line, 8.16–8.74 ka BP)<sup>68</sup>. Light blue shading shows MW4, whereas grey shading indicates the 8.2 ka BP cold event shown in the Greenland Ice Core. Black triangles mark available AMS<sup>14</sup>C dates.

**Changes in the strength of bottom currents.** In addition to the surface water characteristics, some reconstruction of bottom currents has been conducted. Flow speed analysis was investigated via sortable silt mean size ( $\overline{SS}$ ), a direct grain size proxy for the strength of bottom currents<sup>46</sup>.  $\overline{SS}$  values greatly decrease during the HS1 in agreement with increased meltwater discharge

(Fig. 4c, j). During the Bolling warm period,  $\overline{SS}$  values abruptly increase, accompanied by a peak in sedimentation rate (Fig. 4g) probably caused by increased advective supply, i.e., an increase in flow speed, which might reflect a strong DSOW. However, based on the increased accumulation rates (Fig. 3; Supplementary Fig. 2), the velocity is clearly not high enough for net winnowing since 14 ka BP.

Our  $\overline{SS}$  values show a high-amplitude variability during the meltwater events that is difficult to interpret (Fig. 4j), possibly due to the very high detrital suspended matter supply and deposition related to meltwater plumes. However,  $\overline{SS}$  from nearby Core 21GGC exhibits minimum values around 8.5 ka BP, corresponding to low Zr/Rb ratios (proxy for coarse versus fine-grained matter<sup>47</sup>) (Fig. 5c; Supplementary Fig. 5), which suggests probably weakened bottom currents in the Eirik Drift area.  $\overline{SS}$  values show a low-amplitude variability since the last about 8 ka indicate that the strength of bottom currents has been stable and vigorous.

## Discussion

The last deglaciation was characterized by abrupt shifts between cold and warm states in the context of gradually increasing insolation and the decay of the Northern Hemisphere ice sheets, especially the LIS (Fig. 4a). These abrupt events (MW1–MW4) were marked by strong meltwater discharge, rapidly increased sea ice concentration, decreased SSTs, reduced open-water productivity, and probably sluggish bottom currents. During the intervals without strong meltwater discharge, there was no or less sea ice cover, higher SSTs, increased open-water productivity, and stable bottom current intensity. Since the middle Holocene, more stable interglacial conditions characterized by the absence of sea ice, gradually decreasing SSTs, high open-water productivity, and stable and strong bottom currents, were predominant (Figs. 3, 4).

We propose that abrupt changes in sea surface characteristics during the last deglaciation can be attributed to meltwater pulses into the eastern Labrador Sea. During the meltwater events, the peaks in  $\%C_{37:4}$  (i.e., meltwater discharge) correlated with abrupt changes in sea ice cover and SSTs, i.e., low-salinity and low-temperature surface water promoted sea ice formation and decreased SSTs (Fig. 4c–e). These meltwater events exhibited millennial-scale climate fluctuations. Spectral analysis of  $\%C_{37:4}$  record showed high power on a 1560-year cycle (Supplementary Fig. 6), which was similar to 1500-year cycles in Holocene North-Atlantic records (cf., refs. 48,49) and prominent D-O cycles (every 1–2 kyr) during MIS 3<sup>3</sup>. All these cycles showed alternating cold and warm intervals with the cold intervals being related to huge freshwater discharge (this study; ref. 3,48,49). However, D-O cycles were characterized by rapid warming followed by gradual cooling<sup>1–3</sup> and were probably related to a rapid reduction in sea ice in the Nordic Seas<sup>50</sup>, whereas our four meltwater events were marked by abrupt cooling due to abrupt meltwater injection. The beginning and end of these events, i.e., the change from minima to maxima and vice versa, respectively, occurred within a 1–3 cm thick core section. Taken the high sedimentation rate of 100–200 cm/kyr (Fig. 2), this may suggest that the abrupt changes of these millennial-scale events may have occurred within a few decades or even less.

The meltwater pulses into the eastern Labrador Sea were controlled by meltwater discharge from mixed sources. The LIS discharge superimposed by the GrIS (more proximal to the Eirik Drift) was the main source of meltwater discharge. In addition, freshwater/meltwater from the Arctic Ocean might have also contributed to the surface freshening. High dolomite content and increased IRD abundance during MW1 suggest large volumes of meltwater coming from the LIS via iceberg discharge. High detrital carbonate input was also found in the southern Baffin Bay

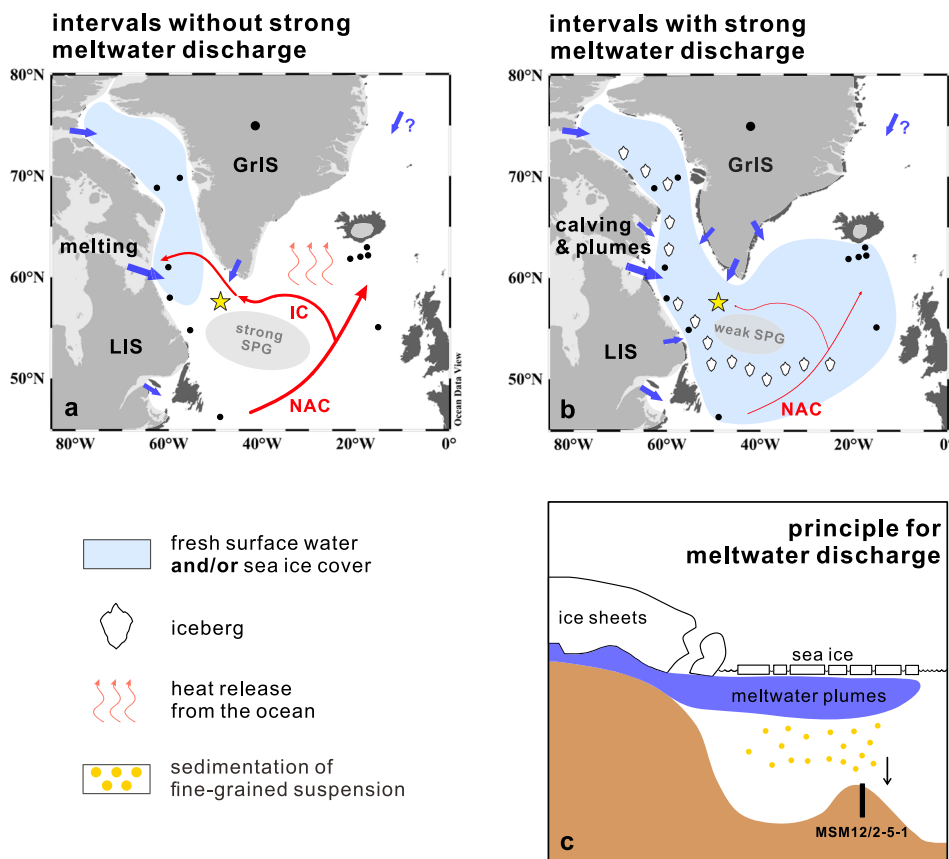


**Fig. 6 Schematic illustration of intervals without/with strong meltwater discharge in the Labrador Sea during the last deglaciation. a** Intervals without strong meltwater discharge preceding the meltwater events: enhanced warm North Atlantic Current (NAC)/Irminger Current (IC) inflow; surface freshening in the Baffin Bay and the northwestern Labrador Sea; **b** Intervals with strong meltwater discharge: weakened NAC/IC inflow; surface freshening in extensive subpolar regions, probably resulting in increased sea ice extent and limited heat release from the ocean. Blue arrows show meltwater discharge: melting of the LIS and the GrIS and possible input from the Arctic Ocean (**a**); calving and meltwater plumes from the LIS and the GrIS and possible input from the Arctic Ocean (**b**). **c** Principal cartoon showing interactions among ice sheet (the LIS and the GrIS) dynamics/meltwater plumes, sea ice formation, and sedimentation of fine-grained suspension during the meltwater events. Yellow star: Core MSM12/2-5-1; black dots: other reference cores.

(Cores SL170 and SL174)<sup>51</sup>, supporting the statement that the LIS prominently collapsed around 14 ka BP. Additionally, increased detrital silicate input (high Si/Sr ratios) meanwhile indicates the GrIS may be also a major contributor to meltwater discharge during this time interval (see bedrock distribution in Fig. 1). During MW2, MW3, and MW4, high detrital silicate and some dolomite input corresponded to detrital carbonate peaks on the Labrador Shelf (Core MD99-2236)<sup>14</sup>, suggesting that such meltwater events were influenced by calving and meltwater plumes from the LIS, superimposed by the GrIS (Fig. 6b, c). No IRD deposition during these time intervals implies that the main route of icebergs transported into the Labrador Sea was probably south of our core location. Furthermore, based on increased continental titanium input between 14 to 10 ka BP from Core MD99-2227<sup>18</sup> and exposure ages of the southern/southwestern/southeastern GrIS<sup>15,16</sup> (Fig. 4h), the GrIS retreated significantly during the last deglaciation, resulting in increased local meltwater discharge towards Eirik Drift during MW1, MW2, and MW3. According to the drainage route and timing, the outburst of Lake Agassiz into the Labrador Sea contributed substantially to the development of MW4, whereas it may be not associated with the other three events<sup>52,53</sup>.

The four meltwater events MW1 to MW4 can be related approximately to cold episodes documented in the Greenland Ice Core record (Fig. 4b–d), suggesting that changes in sea surface

characteristics in the Labrador Sea/subpolar regions may affect wider fluctuations in atmospheric temperature and closely relate to the classical cold events (e.g., YD, and 8.2 ka cold event). In general, and compared to extremely cold intervals (i.e., HS1 and YD), the Bölling/Allerød interval is a relatively warm period shown in NGRIP record<sup>4,54</sup>. However, the Allerød period is a relatively cold interval in contrast to the Bölling warm period<sup>54</sup>, including two major meltwater-related cold phases (the Older Dryas stadial and Intra-Allerød Cold period)<sup>8</sup>. MW1 correlates with lighter  $\delta^{18}O$  during the Allerød period in the NGRIP record (Fig. 4b), decreased (sub-)surface temperatures in the Labrador Sea (this study; ref. <sup>55</sup>) and the northeastern Atlantic<sup>56,57</sup>, surface freshening and reduced ventilation in the North Atlantic<sup>8,58</sup> (Fig. 4e, f; Supplementary Fig. 7). These correlations/similarities indicate that meltwater discharge into the Labrador Sea/subpolar regions might have caused/contributed to the cooling in the high-latitude North Atlantic during the Allerød period. Surface freshening/sea ice expansion in the subpolar regions and following weakened ocean circulation<sup>59</sup> (i.e., limited subpolar gyre and Atlantic Water inflow) could have restricted ocean-atmosphere heat exchange and heat transport northward, resulting in a decline in atmospheric temperatures<sup>50,60</sup>, which may also be applied to the other meltwater events (Fig. 6b). Recent work on the comparison between ice core record and sea ice changes in the Baffin Bay and the Labrador

Sea (Core GS16-204-23CC) during the D-O events provides further evidence that sea ice expansion can greatly affect atmospheric temperatures<sup>61</sup>.

MW2 happened during the late YD, coinciding with the “Heinrich Event 0” (H0) marked by high detrital carbonate input on the Labrador shelf<sup>14</sup> and other North Atlantic areas<sup>62</sup>. Abrupt changes in (sub-)surface temperatures and reduced ocean ventilation in the North Atlantic support that MW2 might have a widespread impact on the subpolar regions (Supplementary Fig. 7). Furthermore, the timing of MW2 was in line with the second distinct weakening of the AMOC during the late YD<sup>63</sup>, suggesting that the disintegration of the LIS and the GrIS might have caused/maintained the cold episode during the late YD, whereas the flooding event in the Arctic Ocean<sup>11,64</sup> might have induced the first phase of AMOC weakening. Therefore, the occurrence of MW2 (H0 event) may explain why the catastrophic outburst of Lake Agassiz during the early YD lasted a few hundred years<sup>11,64</sup> but resulted in a thousand-year cold episode. That means direct freshwater discharge from Lake Agassiz into the Arctic Ocean probably merely triggered the abrupt change during the early YD.

MW3 corresponded to relatively modest changes in the NRGIP record compared to other cold phases (Fig. 4b–d). On the one hand, this might be related to less volumes of meltwater discharge or limited distribution pattern. Thus, prominent changes in surface characteristics were most likely restricted to the proximal Labrador Sea as reflected in distinct decrease in (sub-)surface temperatures in the eastern and southern Labrador Sea (Fig. 4e, f) whereas only modest changes occurred in the more distal northeastern Atlantic (Supplementary Fig. 7). More high-resolution and well-dated records are needed to constrain the distribution pattern. On the other hand, the impact of MW3 on climate may be influenced by the background climate condition. MW3 happened during the late transition phase towards a stable interglacial mode, accompanied by highest insolation and a gradual warming trend, which partially masked the short-term cooling trend caused by inferred meltwater discharge. In comparison to the unstable deglaciation, a larger magnitude and duration of freshwater influx may be required to generate a comparable impact under a relatively stable mode<sup>5,65</sup>. Alternatively, lower sea ice concentration in the Nordic Seas during the early Holocene<sup>66</sup> may have contributed to heat release from the ocean and modest changes in the ice core record.

MW4 that occurred between about 8.74 and 8.33 ka BP, was closely linked to the 8.2 ka BP cold event (Fig. 5). Unfortunately, the exact timing of the peak meltwater discharge cannot be determined in our record due to the limited number of AMS <sup>14</sup>C dates in this time interval. Nevertheless, surface freshening occurred in the Labrador Sea around 8.5 ka BP, consistent with the record from the Labrador Shelf<sup>12,67</sup> and probably caused by the final Lake Agassiz outburst flood<sup>67,68</sup> and collapse of the Hudson Bay Saddle<sup>12</sup>. Based on the correlation between the  $\delta D_{PA}$  values and surface water salinity obtained from Arctic Ocean surface sediments<sup>30</sup>, the  $\delta D_{PA}$  minimum shown in Fig. 5a may represent a salinity anomaly of about -4 for MW4, a tentative statement that has to be approved by further more detailed biomarker and isotope analyses. The onset of meltwater discharge during MW4 was prior to the widespread atmospheric cooling at the 8.2 ka BP cold event, which started about 200 years after the end of MW4. This time difference might be interpreted by the response time between changes in ocean circulation and climate<sup>23</sup>, e.g., such freshening might have perturbed the AMOC about 145–320 yr. and resulted in the 8.2 ka BP cold event<sup>12</sup>. If the Marine 20 calibration curve is used instead of the Marine 13 calibration curve, the 8.2 ka BP cold event occurred during the final stage of MW4 (see Methods and Supplementary Fig. 8). The

abrupt changes in surface characteristics during MW4 (Fig. 5a, b) coincided with distinct minima in the Zr/Rb ratios and the coarse fraction of our Core MSM12/2-5-1 (Fig. 5c) and was consistent with an abrupt decrease in  $\overline{SS}$  values from nearby Core 21GGC, suggesting weakened strength of bottom currents which may reflect a weak DSOW in the Eirik Drift<sup>69</sup> (Supplementary Fig. 5). However, our  $\overline{SS}$  record does not show a clear trend of bottom current variation during the MW4 as well as the other three meltwater events, despite some lowest  $\overline{SS}$  values presence. To further understand bottom current variations and their correlations with changes in sea surface characteristics, a wider range of high-resolution bottom current records over the North Atlantic is needed.

The occurrence of meltwater events was triggered by (sub-) surface ocean warming in the Labrador Sea. Higher SSTs were found in the eastern Labrador Sea preceding high meltwater discharge (i.e., four meltwater events and late HS1) (Fig. 4c, e). *Neogloboquadrina pachyderma* (sin.) is calcifying at the base of the surface mixed layer (50 m depth) in the Eirik Drift region<sup>70</sup>, and our reconstructed temperatures based on Nps-Mg/Ca ratios are quite similar to the  $U_{37}^K$ -based SST values (Fig. 3c). This suggests that the whole upper ocean (surface and subsurface water) was warmer during these periods, possibly caused by enhanced advection of the warm Irminger Current (cf., ref. <sup>71</sup>) (Fig. 6a). Recent research from the southern Labrador Sea<sup>55</sup> shows highly comparable temperature estimates with our SST record and demonstrates that the subsurface warming preceded Heinrich events. Additionally, ocean warming/enhanced Irminger Current has also been proven to be the trigger for surface freshening around 8.5 ka BP in the Labrador Sea (Core MSM45-19-12)<sup>12</sup> (Fig. 5d, e). Our high-resolution records provide new evidence that millennial-scale meltwater events caused by extensive calving of the surrounding LIS and the GrIS were triggered by (sub-)surface ocean warming in the Labrador Sea. Furthermore, rapid sea level rise during the Bølling warm period<sup>72</sup> might also have contributed to basal melting/collapse of ice sheets during the last deglaciation.

In conclusion, our study provides very well-dated and high-resolution proxy records from the eastern Labrador Sea, which could improve our understanding of the impact of meltwater injection into subpolar regions on abrupt climate changes during the last deglaciation. Our new data supports modelling results that higher frequency and amplitude of abrupt changes may occur during the transition states from background climates<sup>5</sup>. We found that meltwater pulses following the collapse of the LIS and GrIS might have triggered millennial-scale abrupt changes in surface freshening and sea ice extent in the Labrador Sea, as well as cooling atmospheric temperatures. These abrupt changes might have occurred within a few decades, which need to be noted in the context of modern accelerating melting of the GrIS and Arctic sea ice due to anthropogenic climate change. Our findings may help to improve model simulations of abrupt changes and predictions of the impact of meltwater discharge on future ocean circulation and climate change.

## Methods

**Chronology.** The age model of Core MSM12/2-5-1 was constrained by 38 Accelerator Mass Spectrometry (AMS) radiocarbon dates of planktic foraminifera *Neogloboquadrina pachyderma* (sinistral). All the AMS <sup>14</sup>C dates were calibrated to calendar years (cal. ka BP) based on the Marine 13 calibration curve<sup>73</sup>, with a global mean reservoir age ( $\Delta R = 0 \pm 200$ ) (see Supplementary Table 1 for details). We used the Marine 13 curve to keep consistency with other published records. We also tested the calibration with the Marine 20 curve<sup>74</sup>, and the results are similar (i.e., the whole records become around 200 years younger) and do not influence our interpretations (Fig. 5; Supplementary Fig. 8). The age-depth model was established on the Bayesian age-modelling (Bacon) approach<sup>75</sup>. The tephra peak



found in 1123 cm core depth and dated to around 12.6 ka BP (based on our current age model) might represent the Vedde Ash layer dated to 12.12 ka BP<sup>32</sup> (Figs. 2, 4i). However, without further geochemical analyses and possible impact from ice-rafted tephra, this tephra layer cannot be attributed to the Vedde Ash layer unambiguously. Furthermore, if this tephra layer is the Vedde Ash layer for sure, this would imply a local reservoir age correction of about 450 years ( $\Delta R = 450$ ) (cf., ref. 76). However, we cannot determine for which time interval this local reservoir age correction has to be considered. Thus, we have not used the Vedde Ash layer as an extra age control point to establish age model, but marked it in Figs. 2 and 4.

**Bulk parameters.** For the measurement of bulk parameters, freeze-dried and homogenized sediments were used. Total organic carbon (TOC) contents were measured by Carbon-Sulfur Analyser (CS-125, Leco) after removing carbonate with hydrochloric acid. Total carbon (TC) contents were determined by Carbon-Nitrogen-Sulfur Analyser (Elementar III, Vario).

**Biomarker analyses.** For biomarker analysis, 5 g of freeze-dried and homogenized sediments were used for extraction by ultrasonication with dichloromethane/methanol (DCM/MeOH, 2:1 v/v). The internal standards 7-hexylnonadecane (7-HND, 0.076 µg), 9-octylheptadec-8-ene (9-OHD, 0.1 µg), 5 $\alpha$ -androstan-3 $\beta$ -ol (androstanol, 10.8 µg), and squalane (3.2 µg) were added prior to the extraction. The extracts were concentrated and separated into hydrocarbon and sterol fraction by open silica gel column chromatography using 5 ml *n*-hexane and 9 ml ethylacetate/*n*-hexane, respectively. Furthermore, the sterol fraction was derivatized with 200 µl bis-trimethylsilyl-trifluoroacet-amid (BSTFA) (60°C, 2h). Hydrocarbons were analysed by gas chromatography/mass spectrometry (GC/MS) (Agilent 7890GC-Agilent 5977 A). Sterols were analysed by GC/MS (Agilent 6850GC-Agilent 5975 A). Compound identification was based on comparison of GC retention times with reference compounds and published mass spectra for highly branched isoprenoids (HBIs) and sterols. HBIs were quantified based on their molecular ions (m/z 350 for IP<sub>25</sub>, m/z 348 for HBI-II, and m/z 346 for HBI-III (Z)) in relation to the fragment ion m/z 266 (7-HND). Brassicasterol (24-methylcholesta-5,22E-dien-3 $\beta$ -ol), campesterol (24-methylcholest-5-en-3 $\beta$ -ol), sitosterol (24-ethylcholest-5-en-3 $\beta$ -ol), and dinosterol (4 $\alpha$ -23,24-trimethyl-5 $\alpha$ -cholest-22E-en-3 $\beta$ -ol) were quantified as trimethylsilyl ethers. Their molecular ions m/z 470, m/z 472, m/z 486, and m/z 500 were used in relation to the molecular ion m/z 348 of the internal standard androstanol. External calibration curves and specific response factors were applied for balancing the different responses of molecular ions of the analytes and the molecular/fragment ions of the internal standards. Biomarker concentrations were normalized based on TOC content of each sample. For analytical details and further references see ref. 77.

Sea ice variations is indicated by the PIP<sub>25</sub> value (Eq. 1), a semi-quantitative index for sea ice reconstruction<sup>27,37</sup>. It is derived from the seasonal sea ice biomarker (IP<sub>25</sub>) and open-water phytoplankton biomarker (e.g., dinosterol, brassicasterol, and HBI-III (Z)). In addition, the C<sub>37</sub> alkenones were also used as phytoplankton marker for PIP<sub>25</sub> calculation.

$$\text{PIP}_{25} = [\text{IP}_{25}] / ([\text{IP}_{25}] + [\text{Phytoplankton biomarker}] \times c) \quad (1)$$

The balance factor *c* corresponds to the ratio of mean concentration of IP<sub>25</sub> and phytoplankton biomarker. In our study, all four PIP<sub>25</sub> proxies based on dinosterol, brassicasterol, HBI-III (Z) and the C<sub>37</sub> alkenones show very similar trends (see data online). Thus, we only used the IP<sub>25</sub>-dinosterol-based PIP<sub>25</sub> to reflect sea ice variations here (Fig. 3b).

As cleaning step for analysing alkenones were necessary, saponification was applied to sterol fraction (see above) using 1 ml 0.1 mol/L KOH (50°C, 12h) before determination of alkenones. Additionally, open silica gel column chromatography was performed using DCM. Internal standard *n*-hexatriacontane (C<sub>36</sub>, 2.1435 µg) was added to each sample for quantification. Alkenones were analysed by GC (Agilent 6890 A) and identified by their retention times and the comparison with an external standard.

The SST reconstruction is based on long-chain C<sub>37</sub> alkenones synthesized by haptophyte algae, using the alkenone unsaturation index (U<sub>37</sub><sup>K</sup>)<sup>28,78</sup>:

$$U_{37}^K = (C_{37:2} - C_{37:4}) / (C_{37:2} + C_{37:3} + C_{37:4}) \quad (2)$$

For calibration of the U<sub>37</sub><sup>K</sup> index to SST values we followed the most recent review study carried out by Filippova et al.<sup>35</sup> for North Atlantic surface sediments, using

$$U_{37}^K = 0.021T + 0.243 \quad (3)$$

Despite U<sub>37</sub><sup>K</sup> not only being affected by SSTs, the regional U<sub>37</sub><sup>K</sup> values still show a high positive correlation with SSTs in the North Atlantic<sup>35</sup>. Furthermore, SST calibration based on U<sub>37</sub><sup>K</sup> (i.e., excluding C<sub>37:4</sub> in the Eq. (2)) exhibits a significant warm bias and more unrealistic SSTs for the North Atlantic<sup>35,41</sup>. The often used SST-alkenones reconstruction based on the global calibration of Müller et al.<sup>79</sup> also displays a larger warm bias at cold temperatures/sea ice cover conditions. A comparison of SST values based on U<sub>37</sub><sup>K</sup> and U<sub>37</sub><sup>S</sup> indices as well as different calibration equations (Rosell-Mele et al.<sup>80</sup>; Müller et al.<sup>79</sup>; Filippova et al.<sup>35</sup>) are presented in online dataset<sup>81</sup>. In the low-temperature range <<10°C, the calibration equation becomes less precise<sup>35</sup>. Thus, the absolute SST values of the

meltwater events should be interpreted more cautiously, and we focus more on the abrupt changes per se.

As a proxy for low temperature and low salinity water, we have used the percentage values of tetra-unsaturated alkenones (%C<sub>37:4</sub>) to indicate meltwater input (cf., ref. 29) following equation:

$$\%C_{37:4} = C_{37:4} / (C_{37:2} + C_{37:3} + C_{37:4}) \times 100 \quad (4)$$

For the analysis of the stable hydrogen isotope composition of palmitic acid ( $\delta D_{PA}$ ), 6g of freeze-dried and homogenized sediments were extracted by ultrasonication with dichloromethane/methanol (DCM/MeOH, 9:1 v/v). The internal standard C19:0 fatty acid (50.5 µg) was added prior to the extraction. The extracts were saponified using 0.1 M KOH in MeOH (50°C, 12h), yielding neutral and acid fractions after hexane extraction and after acidification, respectively. The acid fractions were methylated with MeOH of known isotopic composition (50°C, 12h), yielding the corresponding fatty acid methyl esters (FAMES). The FAME fractions were cleaned by open pipet columns (4 cm silica gel with 0.5 cm Na<sub>2</sub>SO<sub>4</sub>) using DCM.  $\delta D_{PA}$  analyses were carried out on a Thermo Fisher Scientific MAT 253 Isotope Ratio Mass Spectrometer coupled via a GC IsoLink operated at 1420°C to a Thermo Fisher Scientific TRACE GC equipped with a Rxi-5ms column (30 m × 0.25 mm × 0.5 µm). Isotope values were measured against calibrated H<sub>2</sub> gas and  $\delta D$  values are reported in permil against VSMOW. Measurement accuracy was controlled by *n*-alkane standards of known isotopic composition every six measurements. Long-term mean absolute deviation based on the external *n*-alkane standard mixture was 3.0‰. Daily determination of the H<sub>2</sub><sup>+</sup> factor using H<sub>2</sub> as reference gas gave 5.6–5.7, while the precision of the internal standard was 2‰.  $\delta D_{PA}$  values were corrected for the methyl group added during methylation. For analytical details and further reference see ref. 30,82.

**Accumulation rates.** Accumulation rates of bulk parameters and biomarkers were calculated according to the following equations:

$$\text{BAR} = \text{SR} \times \leq (\text{WBD} - 1.026 \times \text{PO}/100) \quad (5)$$

$$\text{MAR} = \text{BAR} \times \text{BM} (\text{or TOC}/100) \quad (6)$$

BAR: bulk sediment accumulation rate (g cm<sup>-2</sup> kyr<sup>-1</sup>); SR: sedimentation rate (cm kyr<sup>-1</sup>); WBD: wet bulk density (g cm<sup>-3</sup>); PO: porosity (%); MAR: mass accumulation rate (g cm<sup>-2</sup> kyr<sup>-1</sup> or µg cm<sup>-2</sup> kyr<sup>-1</sup>); BM: biomarker concentration (µg g<sup>-1</sup>Sed).

**Mg/Ca analysis.** 80 to 200 individuals of *N. pachyderma* (sin.) were picked from the size fraction 150–212 µm for Mg/Ca analysis. Samples were cleaned prior to the measurement. The majority of the Mg/Ca determinations were analysed on the ICP-MS at Cardiff University with an analytical precision for Mg/Ca of ±2% relative standard deviation (RSD) and the remaining samples on the ICP-OES at the Bjerknes Centre for Climate Research with an analytical precision of ±1.4% RSD. The precision for Mg/Ca standard measurements are similar on both the ICP-MS and ICP-OES (<0.9% RSD for long term precision), thus the data from both instruments are interchangeable.

Temperatures were calculated using species-specific *N. pachyderma* (sin.) calibration equation<sup>83</sup>:

$$\text{Mg/Ca} = 0.5 \exp(0.1T) \quad (7)$$

The analytical error of ±2% is equivalent to ±0.2°C using the calibration employed in this study. For analytical details and further references see ref. 84.

**Core MSCL logging and XRF scanning.** During Expedition MSM12/2, hole-core physical property measurements were carried out in the ship laboratory and included non-destructive, continuous determinations of core geometry (diameter), wet bulk density (WBD), P-wave velocity (Vp), and loop sensor magnetic susceptibility (MS) at 10 mm intervals. A standard Multi Sensor Core Logger (MSCL)-S track (GEOTEK Ltd., UK, Ser. No. 25) was used to measure temperature, core diameter, P-wave travel time, gamma-ray attenuation, and MS. The principle of logging cores is described in more detail in the GEOTEK manual “Multi-Sensor Core Logging”, which can be downloaded from the web (<http://www.geotek.co.uk>). The orientation of the P-wave and gamma sensors was horizontal. For further details we refer to the Cruise Report<sup>81</sup>.

The AWI Avaatech XRF (X-Ray Fluorescence) Core Scanner was used for rapid and non-destructive determination of the chemical composition of sediment sections of Core MSM12/2-5-1. Split core surfaces were scanned during a 10 kV, 30 kV, and 50 kV run, in order to obtain reliable intensities (counts per second) of specific major elements. Here we present data of K, Rb, Si, Sr, Ti, and Zr, plotted and interpreted as elemental ratios K/Ti, Si/Sr, and Zr/Rb. For documentation and analytical details, we refer to Avaatech Manual ([https://epic.awi.de/id/eprint/37355/4/XRFCore-Scanner\\_user-manualV2.pdf](https://epic.awi.de/id/eprint/37355/4/XRFCore-Scanner_user-manualV2.pdf)).

**Grainsize analysis: sortable silt.** We analysed the mean size of the non-cohesive sortable silt (SS) fraction (10–63 µm) of 118 samples as a proxy for the strength of bottom water currents<sup>46,85</sup>. Particle sizes <10 µm are predominantly cohesive clay

material deposited as aggregates and thus excluded, as they do not reflect hydrodynamic processes. The method of McCave et al.<sup>46,85</sup> for sortable silt preparation of raw sediments was followed. Approximately 2–4 g of sediments were treated with 250 ml of 2 M acetic acid for carbonate removal and heated at 85 °C for 5 h in 150 ml 2 M sodium carbonate for biogenic silica removal so as to remove biogenic influences on grain size. Samples were then suspended in 0.2% Calgon solution and placed on a rotating wheel for sediment disaggregation followed by 1-min ultrasonic treatment just prior to analysis. Sample size was measured using a Beckman Coulter Multisizer III with a 200 µm aperture.  $\overline{SS}$  mean size measurement errors are  $\pm 2\%$  at sortable silt concentrations  $>5\%$ <sup>86</sup>.

### Data availability

All relevant data in this paper is available at PANGAEA Data Publisher (<https://doi.org/10.1594/PANGAEA.952329>)<sup>81</sup>.

Received: 14 July 2022; Accepted: 3 March 2023;

Published online: 17 March 2023

### References

1. North Greenland Ice Core Project members. High-resolution record of Northern Hemisphere climate extending into the last interglacial period. *Nature* **431**, 147–151 (2004).
2. Dansgaard, W. et al. Evidence for general instability of past climate from a 250-kyr ice-core record. *Nature* **364**, 218–220 (1993).
3. Dokken, T. M., Nisancioglu, K. H., Li, C., Battisti, D. S. & Kissel, C. Dansgaard-Oeschger cycles: interactions between ocean and sea ice intrinsic to the Nordic seas. *Paleoceanography* **28**, 491–502 (2013).
4. Svensson, A. et al. A 60,000 year Greenland stratigraphic ice core chronology. *Clim. Past* **4**, 47–57 (2008).
5. Barker, S. & Knorr, G. Millennial scale feedbacks determine the shape and rapidity of glacial termination. *Nat. Commun.* **12**, 1–12 (2021).
6. Zhang, X. et al. Direct astronomical influence on abrupt climate variability. *Nat. Geosci.* **14**, 819–826 (2021).
7. Denton, G. H. et al. The last glacial termination. *Science* **328**, 1652–1656 (2010).
8. Thornalley, D. J. R., McCave, I. N. & Elderfield, H. Freshwater input and abrupt deglacial climate change in the North Atlantic. *Paleoceanography* **25**, PA1201 (2010).
9. Hemming, S. R. Heinrich events: massive late Pleistocene detritus layers of the North Atlantic and their global climate imprint. *Rev. Geophys.* **42**, RG1005 (2004).
10. Kleiven, H. F. et al. Reduced North Atlantic deep water coeval with the glacial lake agassiz freshwater outburst. *Science* **319**, 60–64 (2008).
11. Keigwin, L. D. et al. Deglacial floods in the Beaufort Sea preceded Younger Dryas cooling. *Nat. Geosci.* **11**, 599–604 (2018).
12. Lochte, A. A. et al. Labrador Sea freshening at 8.5 ka BP caused by Hudson Bay Ice Saddle collapse. *Nat. Commun.* **10**, 1–9 (2019).
13. Margold, M., Stokes, C. R. & Clark, C. D. Reconciling records of ice streaming and ice margin retreat to produce a palaeogeographic reconstruction of the deglaciation of the Laurentide Ice Sheet. *Quat. Sci. Rev.* **189**, 1–30 (2018).
14. Jennings, A., Andrews, J., Pearce, C., Wilson, L. & Ólfasdóttir, S. Detrital carbonate peaks on the Labrador shelf, a 13–7ka template for freshwater forcing from the Hudson Strait outlet of the Laurentide Ice Sheet into the subpolar gyre. *Quat. Sci. Rev.* **107**, 62–80 (2015).
15. Funder, S. et al. Younger Dryas ice margin retreat in Greenland: new evidence from southwestern Greenland. *Clim. Past* **17**, 587–601 (2021).
16. Levy, L. B. et al. Multi-phased deglaciation of south and southeast Greenland controlled by climate and topographic setting. *Quat. Sci. Rev.* **242**, 106454 (2020).
17. Winsor, K., Carlson, A. E., Caffee, M. W. & Rood, D. H. Rapid last-deglacial thinning and retreat of the marine-terminating southwestern Greenland ice sheet. *Earth Planet. Sci. Lett.* **426**, 1–12 (2015).
18. Carlson, A. E., Stoner, J. S., Donnelly, J. P. & Hillaire-Marcel, C. Response of the southern Greenland Ice Sheet during the last two deglaciations. *Geology* **36**, 359–362 (2008).
19. De Vernal, A. & Hillaire-Marcel, C. Sea-ice cover, sea-surface salinity and halo-/thermocline structure of the northwest North Atlantic: Modern versus full glacial conditions. *Quat. Sci. Rev.* **19**, 65–85 (2000).
20. Gibb, O. T., Hillaire-Marcel, C. & de Vernal, A. Oceanographic regimes in the northwest Labrador Sea since Marine Isotope Stage 3 based on dinocyst and stable isotope proxy records. *Quat. Sci. Rev.* **92**, 269–279 (2014).
21. Ruddiman, W. F. Late Quaternary deposition of ice-rafted sand in the subpolar North Atlantic (lat 40° to 65°N). *Bull. Geol. Soc. Am.* **88**, 1813–1827 (1977).
22. Thornalley, D. J. R. et al. A warm and poorly ventilated deep Arctic Mediterranean during the last glacial period. *Science* **349**, 706–710 (2015).
23. Muschitiello, F. et al. Deep-water circulation changes lead North Atlantic climate during deglaciation. *Nat. Commun.* **10**, 1–10 (2019).
24. Hunter, S. et al. Deep western boundary current dynamics and associated sedimentation on the Eirik Drift, Southern Greenland Margin. *Deep. Res. Part I Oceanogr. Res. Pap.* **54**, 2036–2066 (2007).
25. Elliot, M., Labeyrie, L. & Duplessy, J. C. Changes in North Atlantic deep-water formation associated with the Dansgaard-Oeschger temperature oscillations (60–10 ka). *Quat. Sci. Rev.* **21**, 1153–1165 (2002).
26. Belt, S. T. et al. A novel chemical fossil of palaeo sea ice: IP<sub>25</sub>. *Org. Geochem.* **38**, 16–27 (2007).
27. Müller, J. et al. Towards quantitative sea ice reconstructions in the northern North Atlantic: a combined biomarker and numerical modelling approach. *Earth Planet. Sci. Lett.* **306**, 137–148 (2011).
28. Prah, F. G. & Wakeham, S. G. Calibration of unsaturation patterns in long-chain ketone compositions for palaeotemperature assessment. *Nature* **330**, 367–369 (1987).
29. Bard, E., Rostek, F., Turon, J. L. & Gendreau, S. Hydrological impact of Heinrich events in the subtropical Northeast Atlantic. *Science* **289**, 1321–1324 (2000).
30. Sachs, J. P. et al. An Arctic Ocean paleosalinity proxy from  $\delta^2\text{H}$  of palmitic acid provides evidence for deglacial Mackenzie River flood events. *Quat. Sci. Rev.* **198**, 76–90 (2018).
31. Uenzelmann-Neben, G. The expedition of the research vessel "Maria S. Merian" to the Labrador Sea in 2009 (MSM 12/2) Reykjavik-Reykjavik 17. June–13. July 2009. *Reports Polar Mar. Res.* **599**, 1–86 (2009).
32. Abbott, P. M. & Davies, S. M. Volcanism and the Greenland ice-cores: the tephra record. *Earth-Science Rev.* **115**, 173–191 (2012).
33. Mollenhauer, G., McManus, J. F., Wagner, T., McCave, I. N. & Eglinton, T. I. Radiocarbon and <sup>230</sup>Th data reveal rapid redistribution and temporal changes in sediment focussing at a North Atlantic drift. *Earth Planet. Sci. Lett.* **301**, 373–381 (2011).
34. Kolling, H. M. et al. Biomarker distributions in (Sub)-Arctic surface sediments and their potential for Sea Ice reconstructions. *Geochemistry, Geophys. Geosystems* **21**, e2019GC008629 (2020).
35. Filippova, A., Kienast, M., Frank, M. & Schneider, R. R. Alkenone paleothermometry in the North Atlantic: a review and synthesis of surface sediment data and calibrations. *Geochemistry Geophys. Geosystems* **17**, 1370–1382 (2016).
36. Syring, N. et al. Holocene changes in sea-ice cover and polynya formation along the eastern North Greenland shelf: New insights from biomarker records. *Quat. Sci. Rev.* **231**, 106173 (2020).
37. Belt, S. T. et al. Identification of paleo Arctic winter sea ice limits and the marginal ice zone: Optimised biomarker-based reconstructions of late Quaternary Arctic sea ice. *Earth Planet. Sci. Lett.* **431**, 127–139 (2015).
38. Rosell-Melé, A. Interhemispheric appraisal of the value of alkenone indices as temperature and salinity proxies in high-latitude locations. *Paleoceanography* **13**, 694–703 (1998).
39. Bendle, J., Rosell-Melé, A. & Ziveri, P. Variability of unusual distributions of alkenones in the surface waters of the Nordic seas. *Paleoceanography* **20**, PA2001 (2005).
40. Lochte, A. et al. Surface and subsurface Labrador Shelf water mass conditions during the last 6,000 years. *Clim. Past* **16**, 1127–1143 (2020).
41. Wang, K. J. et al. Group 2i Isochrysidales produce characteristic alkenones reflecting sea ice distribution. *Nat. Commun.* **12**, 1–10 (2021).
42. Lecavalier, B. S. et al. A model of Greenland ice sheet deglaciation constrained by observations of relative sea level and ice extent. *Quat. Sci. Rev.* **102**, 54–84 (2014).
43. Leng, W. et al. Sedimentary and rock magnetic signatures and event scenarios of deglacial outburst floods from the Laurentian Channel Ice Stream. *Quat. Sci. Rev.* **186**, 27–46 (2018).
44. Rashid, H., Piper, D. J. W. & Flower, B. P. The role of Hudson Strait outlet in younger Dryas sedimentation in the Labrador Sea. *Geophys. Monogr. Ser.* **193**, 93–110 (2011).
45. Hodell, D. A., Channeil, J. E. T., Curtis, J. H., Romero, O. E. & Röhl, U. Onset of 'Hudson Strait' Heinrich events in the eastern North Atlantic at the end of the middle Pleistocene transition (~640 ka)? *Paleoceanography* **23**, PA4218 (2008).
46. McCave, I. N., Manighetti, B. & Robinson, S. G. Sortable silt and fine sediment size/composition slicing: Parameters for palaeoecurrent speed and palaeoceanography. *Paleoceanography* **10**, 593–610 (1995).
47. Dypvik, H. & Harris, N. B. Geochemical facies analysis of fine-grained siliciclastics using Th/U, Zr/Rb and (Zr + Rb)/Sr ratios. *Chem. Geol.* **181**, 131–146 (2001).
48. Bond, G. et al. A pervasive millennial-scale cycle in North Atlantic Holocene and glacial climates. *Science* **278**, 1257–1266 (1997).

49. Bianchi, G. G. & McCave, I. N. Holocene periodicity in North Atlantic climate and deep-ocean flow south of Iceland. *Nature* **397**, 515–517 (1999).
50. Sadatzki, H. et al. Rapid reductions and millennial-scale variability in Nordic Seas sea ice cover during abrupt glacial climate changes. *Proc. Natl. Acad. Sci. USA* **117**, 29478–29486 (2020).
51. Jackson, R. et al. Asynchronous instability of the North American-Arctic and Greenland ice sheets during the last deglaciation. *Quat. Sci. Rev.* **164**, 140–153 (2017).
52. Teller, J. T., Leverington, D. W. & Mann, J. D. Freshwater outbursts to the oceans from glacial Lake Agassiz and their role in climate change during the last deglaciation. *Quat. Sci. Rev.* **21**, 879–887 (2002).
53. Süfke, F. et al. Arctic drainage of Laurentide Ice Sheet meltwater throughout the past 14,700 years. *Commun. Earth Environ.* **3**, 1–11 (2022).
54. Rasmussen, S. O. et al. A new Greenland ice core chronology for the last glacial termination. *J. Geophys. Res. Atmos.* **111**, D06102 (2006).
55. Max, L., Nürnberg, D., Chiessi, C. M., Lenz, M. M. & Mulitza, S. Subsurface ocean warming preceded Heinrich Events. *Nat. Commun.* **13**, 1–8 (2022).
56. Benway, H. M., McManus, J. F., Oppo, D. W. & Cullen, J. L. Hydrographic changes in the eastern subpolar North Atlantic during the last deglaciation. *Quat. Sci. Rev.* **29**, 3336–3345 (2010).
57. Peck, V. L., Hall, I. R., Zahn, R. & Elderfield, H. Millennial-scale surface and subsurface paleothermometry from the northeast Atlantic, 55–8 ka BP. *Paleoceanography* **23**, PA3221 (2008).
58. Thornalley, D. J. R., Barker, S., Broecker, W. S., Elderfield, H. & McCave, I. N. The deglacial evolution of north atlantic deep convection. *Science*. **331**, 202–205 (2011).
59. Moffa-Sánchez, P. & Hall, I. R. North Atlantic variability and its links to European climate over the last 3000 years. *Nat. Commun.* **8**, 1–9 (2017).
60. Corella, J. P. et al. Climate changes modulated the history of Arctic iodine during the Last Glacial Cycle. *Nat. Commun.* **13**, 1–9 (2022).
61. Scoto, F. et al. Sea ice fluctuations in the Baffin Bay and the Labrador Sea during glacial abrupt climate changes. *Proc. Natl. Acad. Sci. USA* **119**, 1–9 (2022).
62. Andrews, J. T. et al. A Heinrich-like event, H-0 (DC-0): Source(s) for detrital carbonate in the North Atlantic during the Younger Dryas Chronozone. *Paleoceanography* **10**, 943–952 (1995).
63. McManus, J. F., Francois, R., Gherardi, J.-M., Keigwin, L. D. & Brown-Leger, S. Collapse and rapid resumption of Atlantic meridional circulation linked to deglacial climate changes. *Nature* **428**, 834–837 (2004).
64. Wu, J. et al. Deglacial to Holocene variability in surface water characteristics and major floods in the Beaufort Sea. *Commun. Earth Environ.* **1**, 1–12 (2020).
65. Lippold, J. et al. Constraining the Variability of the Atlantic Meridional Overturning Circulation During the Holocene. *Geophys. Res. Lett.* **46**, 11338–11346 (2019).
66. Xiao, X. et al. Deglacial and Holocene sea-ice variability north of Iceland and response to ocean circulation changes. *Earth Planet. Sci. Lett.* **472**, 14–24 (2017).
67. Hoffman, J. S. et al. Linking the 8.2 ka event and its freshwater forcing in the Labrador Sea. *Geophys. Res. Lett.* **39**, 2005–2009 (2012).
68. Barber, D. C. et al. Forcing of the cold event of 8,200 years ago by catastrophic drainage of Laurentide lakes. *Nature* **400**, 344–348 (1999).
69. Henderson, S. S. *Tracking Deep-Water Flow On Eirik Drift Over The Past 160 Kyr: Linking Deep-Water Changes To Freshwater Fluxes* (Doctoral dissertation, Rutgers The State University of New Jersey, 2009).
70. Jonkers, L., Brummer, G. J. A., Peeters, F. J. C., Van Aken, H. M. & De Jong, M. F. Seasonal stratification, shell flux, and oxygen isotope dynamics of leftcoiling *N. pachyderma* and *T. quinqueloba* in the western subpolar North Atlantic. *Paleoceanography* **25**, PA2204 (2010).
71. Seidenkrantz, M. S. et al. Evidence for influx of Atlantic water masses to the Labrador Sea during the Last Glacial maximum. *Sci. Rep.* **11**, 1–14 (2021).
72. Lambeck, K., Rouby, H., Purcell, A., Sun, Y. & Sambridge, M. Sea level and global ice volumes from the Last Glacial Maximum to the Holocene. *Proc. Natl. Acad. Sci. USA* **111**, 15296–15303 (2014).
73. Reimer, P. J. et al. IntCal13 and Marine13 radiocarbon age calibration curves 0–50,000 years cal BP. *Radiocarbon* **55**, 1869–1887 (2013).
74. Heaton, T. J. et al. Marine20 - the marine radiocarbon age calibration curve (0–55,000 cal BP). *Radiocarbon* **62**, 779–820 (2020).
75. Blaauw, M. & Christen, J. A. Flexible paleoclimate age-depth models using an autoregressive gamma process. *Bayesian Anal.* **6**, 457–474 (2011).
76. Austin, W. E. N., Bard, E., Hunt, J. B., Kroon, D. & Peacock, J. D. The <sup>14</sup>C age of the Icelandic Vedde Ash: implications for Younger Dryas marine reservoir age corrections. *Radiocarbon* **37**, 53–62 (1995).
77. Fahl, K. & Stein, R. Modern seasonal variability and deglacial/Holocene change of central Arctic Ocean sea-ice cover: New insights from biomarker proxy records. *Earth Planet. Sci. Lett.* **351–352**, 123–133 (2012).
78. Brassell, S. C., Eglinton, G., Marlowe, I. T., Pflaumann, U. & Sarnthein, M. Molecular stratigraphy: A new tool for climatic assessment. *Nature* **320**, 129–133 (1986).
79. Müller, P. J., Kirst, G., Ruhland, G., Von Storch, I. & Rosell-Melé, A. Calibration of the alkenone paleotemperature index U<sub>37</sub> based on core-tops from the eastern South Atlantic and the global ocean (60°N–60°S). *Geochim. Cosmochim. Acta* **62**, 1757–1772 (1998).
80. Rosell-Melé, A., Eglinton, G., Pflaumann, U. & Sarnthein, M. Atlantic core-top calibration of the U<sub>37</sub> index as a sea-surface palaeotemperature indicator. *Geochim. Cosmochim. Acta* **59**, 3099–3107 (1995).
81. You, D. et al. Biomarker, bulk parameter, XRF data of sediment core MSM12/2-5-1 from the Labrador Sea. *PANGAEA* <https://doi.org/10.1594/PANGAEA.952329> (2022).
82. Häggi, C., Chiessi, C. M. & Schefuß, E. Testing the D/H ratio of alkenones and palmitic acid as salinity proxies in the Amazon Plume. *Biogeosciences* **12**, 7239–7249 (2015).
83. Elderfield, H. & Ganssen, G. Past temperature and δ<sup>18</sup>O of surface ocean waters inferred from foraminiferal Mg/Ca ratios. *Nature* **405**, 442–445 (2000).
84. Williams, M. C. *The Pelagic Record of Ocean Acidification* (Doctoral dissertation, University of Bristol, 2015).
85. McCave, I. N. & Hall, I. R. Size sorting in marine muds: processes, pitfalls, and prospects for paleoflow-speed proxies. *Geochemistry, Geophys. Geosystems* **7**, Q10N05 (2006).
86. Bianchi, G. G., Hall, I. R., McCave, I. N. & Joseph, L. Measurement of the sortable silt current speed proxy using the Sedigraph 5100 and Coulter Multisizer IIe: Precision and accuracy. *Sedimentology* **46**, 1001–1014 (1999).
87. Simon, Q., Hillaire-Marcel, C., St-Onge, G. & Andrews, J. T. North-eastern Laurentide, western Greenland and southern Inuitian ice stream dynamics during the last glacial cycle. *J. Quat. Sci.* **29**, 14–26 (2014).
88. Andrews, J. T. & Voelker, A. H. L. “Heinrich events” (& sediments): a history of terminology and recommendations for future usage. *Quat. Sci. Rev.* **187**, 31–40 (2018).
89. Peltier, W. R., Argus, D. F. & Drummond, R. Space geodesy constrains ice age terminal deglaciation: the global ICE-6G\_C (VM5a) model. *J. Geophys. Res.* *Solid Earth* **120**, 450–487 (2015).
90. Laskar, J. et al. A long-term numerical solution for the insolation quantities of the Earth. *Astron. Astrophys.* **428**, 261–285 (2004).

## Acknowledgements

We sincerely thank the professional support of the captain and crew of the R/V *Maria S. Merian* as well as the scientific team on the expedition MSM12/2. We also thank W. Lutter for technical assistance with the measurement at AWI. Many thanks to G. Mollenhauer, the AWI MICADAS lab, and S. Morton (SUERC) for radiocarbon measurement. Thanks to C. Vogt for XRD analysis. This project was supported by the Deutsche Forschungsgemeinschaft (DFG) through the International Research Training Group IRTG 1904 ArcTrain. Grant NE/I020261/1 from NERC in the ocean acidification program to D.N.S. is also gratefully acknowledged. Furthermore, we acknowledge support by the Open Access Publication Funds of AWI.

## Author contributions

R.S. designed this study. R.S. and D.N.S. contributed to the fieldwork and sampling. D.Y. and K.F. conducted biomarker analyses, evaluation, and quality control. D.Y. and M.C.W. prepared foraminifera samples for radiocarbon measurement. D.Y. carried out bulk parameters and coarse fraction analyses. F.N. and G.K. performed MSCL logging and XRF scanning, respectively. M.C.W., D.N.S., I.N.M., and S.B. generated and evaluated sortable silt and Mg/Ca ratios of foraminifera. D.Y. carried out the extraction of palmitic acid. E.S. conducted hydrogen isotope measurements of palmitic acid and evaluation. D.Y. wrote the manuscript with input from R.S., D.N.S., I.N.M., S.B., and L.N. All the co-authors contributed to the data interpretation and writing the final version of the paper.

## Funding

Open Access funding enabled and organized by Projekt DEAL.

## Competing interests

The authors declare no competing interests.

## Additional information

**Supplementary information** The online version contains supplementary material available at <https://doi.org/10.1038/s43247-023-00743-3>.

**Correspondence** and requests for materials should be addressed to Defang You.

**Peer review information** *Communications Earth & Environment* thanks the anonymous reviewers for their contribution to the peer review of this work. Primary Handling Editors: Kyung-Sook Yun and Joe Aslin. Peer reviewer reports are available.

**Reprints and permission information** is available at <http://www.nature.com/reprints>

**Publisher's note** Springer Nature remains neutral with regard to jurisdictional claims in published maps and institutional affiliations.



**Open Access** This article is licensed under a Creative Commons Attribution 4.0 International License, which permits use, sharing, adaptation, distribution and reproduction in any medium or format, as long as you give appropriate credit to the original author(s) and the source, provide a link to the Creative Commons license, and indicate if changes were made. The images or other third party material in this article are included in the article's Creative Commons license, unless indicated otherwise in a credit line to the material. If material is not included in the article's Creative Commons license and your intended use is not permitted by statutory regulation or exceeds the permitted use, you will need to obtain permission directly from the copyright holder. To view a copy of this license, visit <http://creativecommons.org/licenses/by/4.0/>.

© The Author(s) 2023